



Ultrathin PdPt bimetallic nanowires with enhanced electrocatalytic performance for hydrogen evolution reaction



Hao Lv^{a,1}, Xin Chen^{b,1}, Dongdong Xu^{a,*}, Yichen Hu^a, Haoquan Zheng^c, Steven L. Suib^{d,*}, Ben Liu^{a,*}

^a Jiangsu Key Laboratory of New Power Batteries, Collaborative Innovation Center of Biomedical Functional Materials, School of Chemistry and Materials Science, Nanjing Normal University, Nanjing 210023, China

^b Center for Genome Technology and Biomolecular Engineering, Department of Chemical Engineering, Columbia University, New York City, NY 10027, United States

^c Key Laboratory of Applied Surface and Colloid Chemistry, Ministry of Education, School of Chemistry and Chemical Engineering, Shaanxi Normal University, Xi'an, Shaanxi 710119, China

^d Department of Chemistry and Institute of Materials Science, University of Connecticut, Storrs, CT 06269, United States

ARTICLE INFO

Keywords:

Ultrathin nanowires
Bimetallic PdPt
Synergistic effect
Electrocatalysis
Hydrogen evolution reaction

ABSTRACT

We report a general bottom-up synthetic methodology to epitaxially grow 3-nm-thick single-crystalline PdPt bimetallic nanowires using amphiphilic dioctadecyldimethylammonium chloride as the surfactant template. Mechanistic studies show that the existence of Pd element is critical in the synthesis of bimetallic PdPt nanowires with controllable atomic ratios. Due to synergistic effect of anisotropic single-crystalline ultrathin one-dimensional nanostructures and bimetallic elemental compositions, the resulting PdPt nanowires exhibit superior electrocatalytic activity and stability towards the hydrogen evolution reaction (HER). Among them, bimetallic Pd₈₆Pt₁₄ nanowires show the best HER activity with a small overpotential of only 0.8 mV in acidic media at a current density of 10 mA/cm² (12.8 mV positive than that of commercial Pt nanoparticles), and excellent stability with only 4.6% loss in activity after current-time chronoamperometric responses for 26 h. This surfactant template-directing approach opens a general method for precise control of anisotropic nanostructures in diverse bimetallic nanomaterials for the high-performance electrocatalysts.

1. Introduction

Rational design and synthesis of metal nanocrystals with well-controlled nanostructures and shapes are of great importance in the electrocatalysis [1–6]. Among these, noble metal nanocrystals, especially Pt with diverse nanostructures and compositions, have received particular interest due to their excellent electrocatalytic performances in the hydrogen evolution reaction (HER) [7], the oxygen reduction reaction (ORR) [8–10], and alcohol or formic acid oxidation reaction [11]. However, such Pt nanocatalysts generally possess relatively high cost and poor electrocatalytic durability, and thus hamper extensive applications [12]. One general solution is to dope secondary metals (for example Pd in Pt) for formation of bimetallic counterparts [13,14], in which bifunctional and electronic effects of two metal elements efficiently improve their electrocatalytic activity and stability by optimizing the binding energy of absorbed hydrogen (for HER) [7] or oxygen (for ORR) [8,10,15,16]. In addition, the utilization efficiency of

noble metals can be enhanced by alloying with cheaper secondary metals [17–21]. On the other hand, constructing asymmetric one-dimensional (1D) single-crystalline ultrathin nanoarchitectures has also been utilized recently as an alternative strategy to enhance the electrocatalytic performance [21–27], in which structurally anisotropic features greatly enhance contraction affinity of metal nanocrystals with carbon support/electrode materials and suppress physical Ostwald ripening processes during the electrocatalysis. Meanwhile, anisotropic single-crystalline 1D nanostructures with ultrathin thickness also partially improve atomic utilization efficiency and facilitate electron transfer, and thus enhance electrocatalytic activity kinetically [28]. Ultrathin 1D bimetallic PdPt nanowires are a good match to the above features, including anisotropic single-crystalline 1D nanostructure, bimetallic composition, and high utilization efficiency of surface noble metal atoms. However, the synthesis of such ultrathin single-crystalline PdPt nanowires with a thickness sub-3 nm is technically challenging, especially in aqueous solution, due to the symmetric face-centered

* Corresponding authors.

E-mail addresses: ddxu@njnu.edu.cn (D. Xu), steven.suib@uconn.edu (S.L. Suib), ben.liu@njnu.edu.cn (B. Liu).

¹ These authors contributed equally to this work.

cubic (fcc) crystallographic orientations and different crystallization growth processes of Pt and Pd [29–34].

In the current manuscript, we report a facile yet powerful one-step synthetic strategy to grow *in situ* 3-nm-thick 1D single-crystalline ultrathin PdPt bimetallic nanowires and precisely control their atomic ratios using a surfactant-directing solution-phase method. Dioctadecyldimethylammonium chloride (DODAC) with double hydrophobic tails and one hydrophilic head was chosen as the surfactant template to stabilize and direct the self-assembly with two different metal precursors into hexagonal columnar mesophases in aqueous solution, and further confine the crystallization growth of bimetallic nanocrystals between mesochannels of columnar nanoreactors by *in situ* chemical reduction. Epitaxial growth of two metal nanocrystals along mesoscopic columnar direction thus results in the formation of ultrathin single-crystalline bimetallic nanowires. Due to ultrathin 1D anisotropic feature, single-crystalline nature, and synergistic effect of bimetallic composition, the resulting PdPt nanowires exhibited superior HER activity in both acid and alkaline solution, and excellent stability with only 4.6% loss in activity after testing for 26 h.

2. Experimental

2.1. Chemicals

Commercial palladium and platinum nanoparticles (PdNPs and PtNPs), palladium (II) chloride (PdCl_2 , 99.9%), chloroplatinic acid (H_2PtCl_6 , 99.9%), DODAC, acetic acid and L-ascorbic acid (AA) were purchased from Alfa Aesar. Ethanol, hydrochloric acid (HCl), and sodium hydroxide (NaOH) were obtained from Sinopharm Chemical Reagent Co. Ltd. (Shanghai). Nafion solution was from Sigma Aldrich. 10 mM of H_2PdCl_4 solution was prepared by dissolving 0.18 g of palladium (II) chloride in 10 mL of HCl solution (0.2 M) and further diluting to 100 mL with deionized water (DI H_2O). All the reagents were of analytical reagent grade and used without further purification. DI H_2O used in the work has a resistivity of 18.25 mΩ.

2.2. Synthesis of ultrathin PdPt bimetallic nanowires

Ultrathin single-crystalline PdPt bimetallic nanowires were synthesized by a solution-phase route using DODAC as the template, H_2PdCl_4 and H_2PtCl_6 as metal precursors, and AA as the reducing agent. Taking the sample with a feed ratio of 20% as an example, 30 mg of DODAC was totally dissolved in 10 mL of DI H_2O , then 0.8 mL of H_2PdCl_4 solution (10 mM) and 0.2 mL of H_2PtCl_6 (10 mM) were successively added to the above solution. The resultant solution was then kept at 95°C for 30 min to drive the self-assembly of DODAC/metal hybrids. After that, 1.0 mL of freshly prepared 0.3 M AA was rapidly injected, following the prompt color change of the solution from light pink to dark brown. The solution was kept at 95°C for an additional 30 min. Lastly, ultrathin PdPt bimetallic nanowires were collected by centrifugation and washed several times with ethanol/DI H_2O . Similarly, PdPt bimetallic nanowires with different molar ratios as well as pure Pd nanowires and PtNPs were synthesized using the same procedures by changing the feed ratios of Pd to Pt.

2.3. Electrochemical measurement

Electrocatalytic studies were carried out on a CHI 660E electrochemical analyser at 25 °C. A three-electrodes system was used for all electrochemical tests, which consisted of a carbon rod as the counter electrode, a saturated calomel electrode as the reference electrode, and a glassy carbon electrode (GCE, 0.07065 cm²) as the working electrode. Before electrocatalytic tests, the nanocatalysts were first washed with acetic acid and DI H_2O for three times to remove the surfactants and impurities on the nanowires [35]. Typically, a nanocatalyst ink was prepared by mixing 1 mg of nanocatalysts, 4 mg of carbon black (Valcan

XC-72), 1 mL of ethanol/DI H_2O (8:2 by volume). After sonicating for > 30 min, 50 μL of Nafion solution was mixed and further sonicated for an additional 30 min. Then, 6 μL of the ink solution (~6 μg of the catalyst) was casted on GCE and dried at 40 °C before test. Linear sweep voltammetry (LSV) curves were obtained at 0.5 M H_2SO_4 and 1.0 M KOH with a scan rate of 5 mV s⁻¹, while cyclic voltammetry (CV) curves were collected at 0.5 M H_2SO_4 with a scan rate of 50 mV/s. All results were obtained by IR compensation (5%) and all reported potentials in this work were referenced to the reversible hydrogen electrode (RHE). Electrochemical impedance spectra (EIS) measurements were performed with an AutoLab with 0.5 M H_2SO_4 at open circuit potentials with the frequency in the range of 0.1 Hz and 10, 000 Hz with the sinusoidal perturbation fixed potential of 30 mV.

Electrochemically active surface areas (ECSAs) were calculated from the CV curves according to the following equation:[36,37]

$$\text{ECSA} = \frac{Q}{C \cdot m}$$

Where Q is the Coulombic charge of the hydrogen desorption peak area, C is the hydrogen adsorption constant, and m is the mass of the catalyst (Pd, Pt and PdPt). For Pd, C = 4.2 C/m²; for Pt, C = 2.1 C/m²; and for Pd_xPt_y , C = 4.2x/(x + y) + 2.1y/(x + y).

2.4. Characterizations

Transmission electron microscopy (TEM) and high-resolution TEM images were collected using a JEOL 2010 at an accelerating voltage of 200 kV. High-angle annular dark-field scanning STEM was carried out using a Talos F200X Atomic Resolution Analytical Microscope. TEM and STEM samples were prepared by casting a suspension (ethanol) of the samples on TEM grids directly. X-ray diffraction (XRD) patterns were performed on powder samples using a D/max 2500 V L/PC diffractometer equipped with graphite-monochromatized Cu Kα radiation in the 2θ ranging from 30° to 90°. Related working voltages and currents are 40 kV and 100 mA, respectively. X-ray photoelectron spectra (XPS) were performed on a scanning X-ray microprobe (Thermo ESCALAB 250Xi) that uses Al Kα radiation. All samples were directly characterized without carbon support, except for electrocatalytic tests.

3. Results and discussion

3.1. Synthesis and structural characterizations of ultrathin PdPt bimetallic nanowires

The synthetic routes of ultrathin PdPt bimetallic nanowires using the surfactant-directing method in an aqueous solution is schematically illustrated in Fig. 1a. In a typical synthesis, amphiphilic surfactant of DODAC was totally dissolved in DI H_2O following the addition of two noble metal precursors (H_2PdCl_4 and H_2PtCl_6). By means of electrostatic interactions between cationic quaternary ammonium groups in DODAC and anionic inorganic metal precursors (PdCl_4^{2-} and PtCl_6^{2-}), a mesophase with a hexagonal p6mm nanostructure can be assembled and formed immediately through well-known cooperative self-assembly processes (Fig. S1) [38]. Then, AA as the reducing agent was introduced into the synthetic system for *in situ* co-reduction of two metal precursors simultaneously into bimetallic PdPt nanowires between nanoconfined cylindrical mesophases. The color of the reaction solution quickly changed into dark-brown with obvious Tyndall effect, implying the formation of PdPt nanocrystals (see picture inserted in Fig. 1b). Our synthetic process is pretty simple in one step, and can be promptly finished in several minutes. The presence of DODAC is a key factor for the formation of ultrathin PdPt nanowires, due to the strong hydrophobic effect between double long-chain hydrophobic tails. In contrast, no nanowire structure can be obtained when using surfactants with single hydrophobic carbon chains, such as cetylpyridinium chloride and cetyltrimethylammonium chloride [38,39].

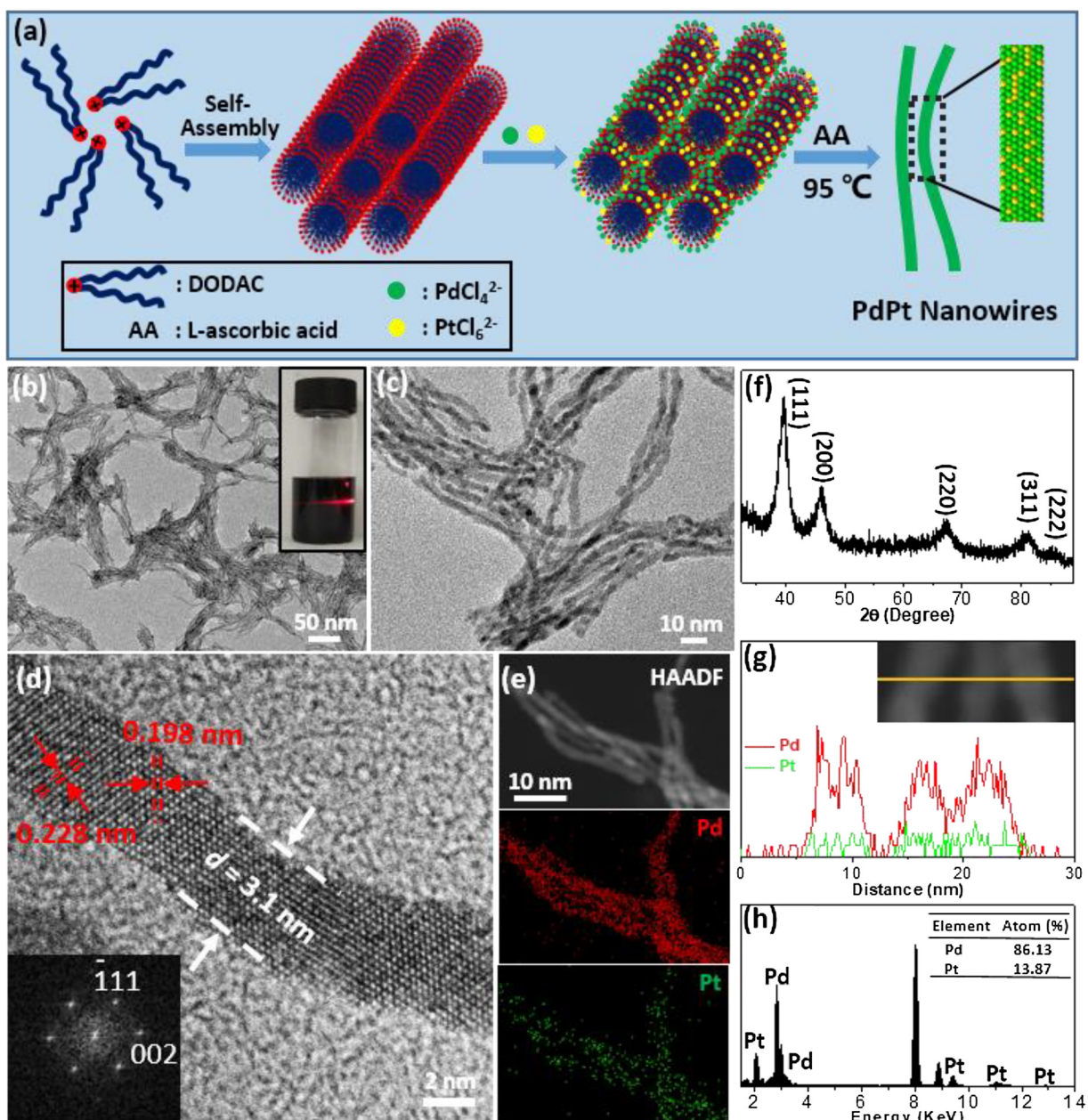


Fig. 1. Synthesis and structural characterization of bimetallic PdPt nanowires. (a) Schematic illustration for the formation routes of bimetallic PdPt nanowires. (b) Low-magnification, (c) high-magnification and (d) high-resolution TEM images, and (e) STEM mapping of bimetallic Pd₈₆Pt₁₄ nanowires. Inserted in (b) is the digital picture of ultrathin PdPt nanowires (in solution). (f) Wide-angle XRD, (g) STEM line scan and (h) STEM-EDX of Pd₈₆Pt₁₄ nanowires.

As-made ultrathin Pd₈₆Pt₁₄ bimetallic nanowires were carefully characterized by TEM as an example, as Pd₈₆Pt₁₄ nanowires exhibited the best HER activity in acidic media among all PdPt nanowires with different atomic ratios (see below). As shown in Fig. 1b, the typical low-magnification TEM images clearly showed highly dispersed nanowires with a high purity and uniformity. The nanowires were straight with very smooth surfaces, and no interconnected crystal networks were observed. High-magnification TEM images (Fig. 1c) indicated the sample composed of ultrathin nanowires with an average diameter of 3.1 nm (Fig. 1d) and an ultralong length in the range of 100–300 nm (see more TEM images in Fig. S2). The high-resolution TEM image exhibited two lattice spacings of 0.228 and 0.198 nm, indicating that PdPt nanowires were dominated by the (111) and (002) planes of fcc crystallographic orientation (Fig. 1d). The clear high-resolution TEM observations suggested that the nanowires were nearly single-crystalline, as indicated by lattice fringes aligned along the same orientation.

The single crystalline feature of PdPt nanowires was also confirmed when checking the high-resolution TEM images in three different domains in a single PdPt nanowire (Fig. S3). The successful synthesis of bimetallic PdPt nanowires was also confirmed by HAADF-STEM (Fig. 1e). Both Pd and Pt elements were homogeneously dispersed along the nanowire framework, indicating a bimetallic alloyed feature (see more STEM images in Fig. S4). STEM line scan analysis further implied that the resultant PdPt nanowires were bimetallic (Fig. 1g). The crystalline nature of the PdPt nanowires was also confirmed by wide-angle XRD (Fig. 1f). Five typical peaks can be indexed as the (111), (200), (220), (311), and (222) reflections of typical fcc nanocrystals. STEM energy-dispersive X-ray spectroscopy (EDX) showed the typical peaks corresponding to Pd and Pt (Fig. 1h) with the average molar ratio of Pd to Pt of 86:14 (defined as Pd₈₆Pt₁₄ hereafter). Survey XPS showed the nanowires were composed of Pd and Pt with an atom ratio of 85:15 (Fig. S5), almost the same as that from STEM-EDX. Above observations

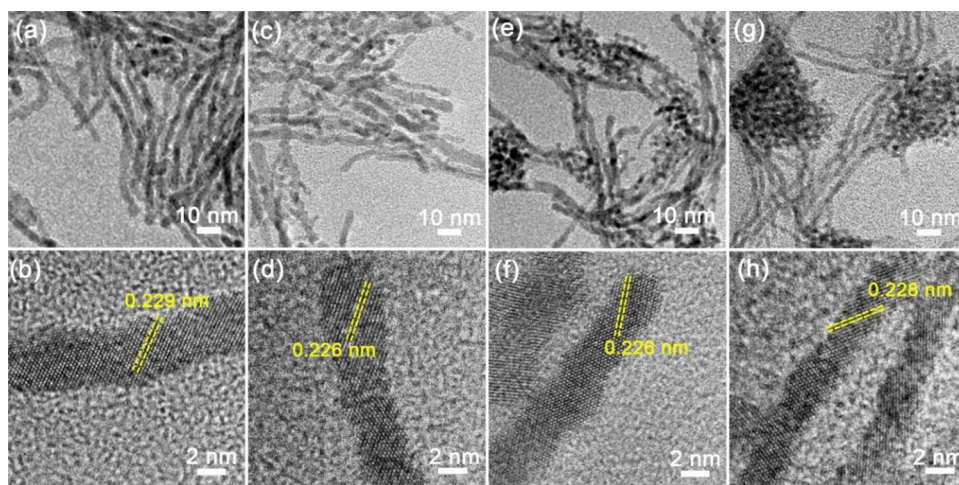


Fig. 2. Morphological control of bimetallic PdPt nanowires. Typical TEM and high-resolution TEM images of (a, b) monometallic Pd, (c, d) bimetallic Pd₇₇Pt₂₃, (e, f) Pd₆₁Pt₃₉, and (g, h) Pd₄₆Pt₅₄ nanowires.

definitely exhibit successful growth of 3-nm-thick single-crystalline Pd₈₆Pt₁₄ bimetallic nanowires.

3.2. Tuning elemental component of Pd and Pt in bimetallic PdPt nanowires

The elemental component and corresponded synergistic effects of bimetallic PdPt nanocrystals are the key to boost their electrocatalytic performances [40]. In our synthetic system, the atomic ratios of ultra-thin PdPt bimetallic nanowires were readily tuned by changing the feed ratios of two noble metal precursors. The structural evolution of bimetallic nanowires was summarized in Figs. 2 and S6 (see Figs. S7–S15 for more TEM details). When the feed ratio of Pd to Pt is higher than 4:1 (20 at % of Pt), well-defined PdPt bimetallic nanowires were obtained irrespective of the ratio of metal precursors. However, the real atomic ratio of Pd to Pt was slightly higher than the feed ratio (Fig. S6). For example, 1.5, 3.5, 6.7 and 14 at % of Pt was achieved in resultant PdPt nanowires (denoted as Pd_{98.5}Pt_{1.5}, Pd_{96.5}Pt_{3.5}, Pd_{93.3}Pt_{6.7} and Pd₈₆Pt₁₄) when the feed amount of Pt was 2.5, 5, 10, and 20 at %, respectively (Figs. S8–S10). The results indicated that Pd is preferentially reduced and Pt is not totally reduced in the synthesis process, because of the different reduction abilities of PtCl₆²⁻ and PdCl₄²⁻ using AA as a reducing agent [41]. In our experiments, the slower reduction speed of PtCl₆²⁻ (> 20 at% of Pt) resulted ultralong nanowires in shorted ones, and finally in disordered shapes (larger nanoparticles (NPs) and the aggregates of these NPs, see high-resolution TEM in Fig. S16). When decreasing the feed ratio to 70:30, however, small amounts of irregular nanoparticles appeared gradually, although most of the samples were still nanowires (Pd₇₇Pt₂₃, Fig. 2c and d, also Fig. S11). Meanwhile, the nanowires became shorter (50–200 nm) and slightly thicker (2–3 nm). When continuously decreasing the feed ratio to 60:40, 50:50 and 33:67, the fractions of NPs and corresponding aggregates of PdPt NPs dramatically increased (Pd₆₁Pt₃₉, Pd₄₆Pt₅₄, Fig. 2e, f, g, h and Figs. S12–S14), indicating that the introduction of excessive Pt into the Pd nanowire system would intrinsically change the reduction kinetics and resultant nanostructures. This result was also confirmed by the synthesis of monometallic Pt nanostructures using the same procedures. Only NPs can be observed when using H₂PtCl₆ as sole precursor (Fig. S15).

Wide-angle XRD was used to further investigate the crystalline structure, especially bimetallic feature (no phase separation), of PdPt nanowires (Fig. 3). As shown in Fig. 3a, only five typical XRD peaks (single set) were observed for all PdPt nanowires, indicating the formation of bimetallic alloys. With the introduction of Pt into Pd nanowires, a minimum impact on fcc Pd was implied during the synthesis of bimetallic PdPt alloys. However, a very small shift in (111) planes to

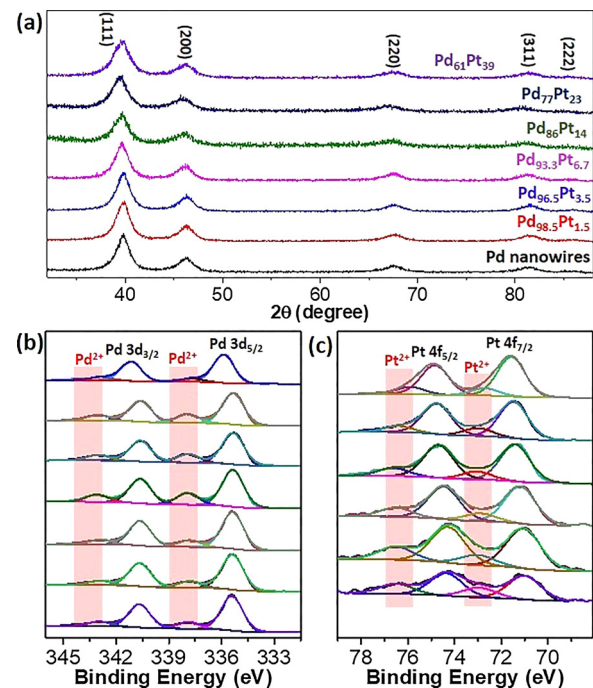


Fig. 3. Structural evolution of bimetallic PdPt nanowires. (a) Wide-angle XRD patterns, (b) high-resolution XPS Pd 3d and (c) Pt 4f spectra of PdPt nanowires. From bottom to up is monometallic Pd nanowires, bimetallic Pd_{98.5}Pt_{1.5}, Pd_{96.5}Pt_{3.5}, Pd_{93.3}Pt_{6.7}, Pd₈₆Pt₁₄, Pd₇₇Pt₂₃, and Pd₆₁Pt₃₉ nanowires, respectively.

lower degree ($\sim 0.2^\circ$) can be found on increasing the content of Pt, indicating a slight change in lattice constant. Considering the slightly larger atom size of Pt, the changes revealed the formation of alloyed bimetallic nanostructure based on the incorporation of Pt in fcc Pd [42,43].

The successful synthesis of bimetallic PdPt nanowires was also confirmed by high-resolution XPS Pd 3d and Pt 4f spectra. In contrast to monometallic Pd nanowires, the Pd 3d peak of bimetallic PdPt nanowires exhibited an obvious shift towards higher energy. Moreover, very small amounts of Pd²⁺ (< 5%) were also observed when the amount of Pt is lower. Among them, the shifts of both Pd 3d_{3/2} and 3d_{5/2} increased along with a larger amount of Pt (Fig. 3b). Similarly, down-shifts in Pt 4f were also observed on decreasing the amount of Pt in bimetallic PdPt nanowires (Fig. 3c). Meanwhile, the amount of Pt²⁺ also slightly

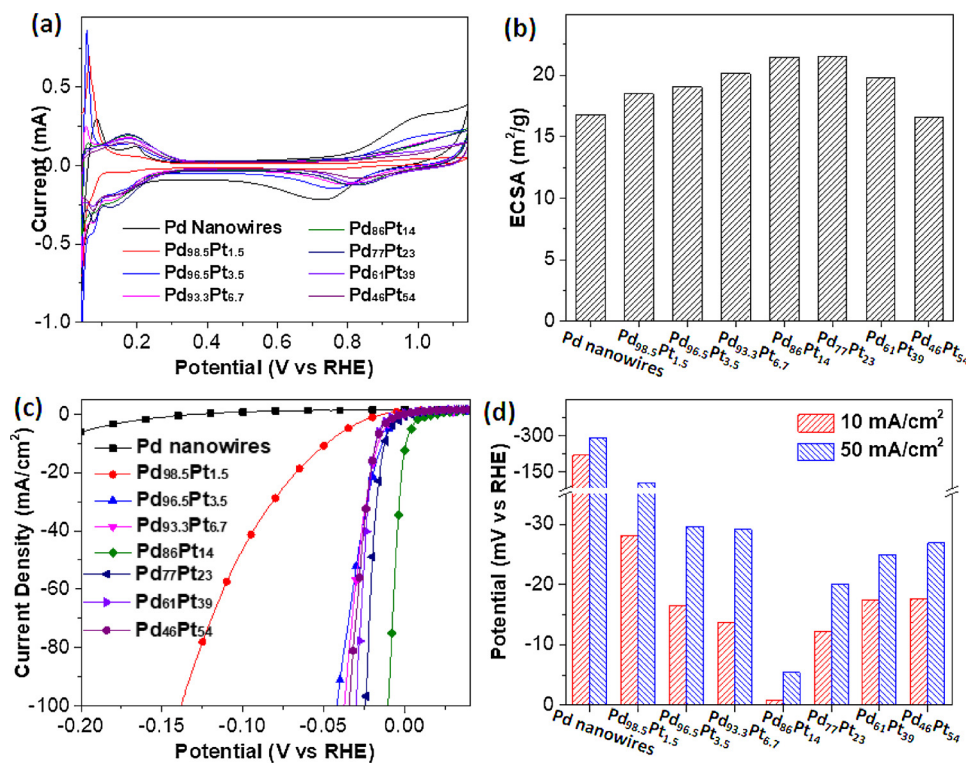


Fig. 4. Electrocatalytic HER activities of ultrathin PdPt bimetallic nanowires with different Pt contents. (a) CV curves and (b) summarized ECSAs of PdPt nanowires in 0.5 M H₂SO₄ at a scan rate of 50 mV/s. (c) LSV curves and (d) summarized electrocatalytic activities of PdPt nanowires in 0.5 M H₂SO₄ at a scan rate of 5 mV/s.

decreased with an increase of Pt content. Both shifts in Pd and Pt as well as the existence of Pd²⁺/Pt²⁺ were ascribed to the formation of Pd-Pt interactions, which changed the electronic structure of Pd by alloying with Pt [10,43,44]. The obviously changed electronic states of Pd and Pt in ultrathin PdPt bimetallic nanowires may result in bifunctional and electronic effects of both Pd and Pt, which intrinsically enhance their electrocatalytic performances [7,8,10,43].

3.3. Electrocatalytic HER performance of bimetallic PdPt nanowires

Electrocatalytic HER was investigated to evaluate the activity and stability of ultrathin PdPt bimetallic nanowires in both acidic and alkaline conditions, and commercial PtNPs and PdNPs were also compared as controls. We first performed cyclic voltammetry (CV) tests in a three-electrodes system at 0.5 M H₂SO₄ with a scan rate of 50 mV/s, to reveal their intrinsic electrochemical behaviour. As shown in Fig. 4a, a typical pair of peaks, which were ascribed to the adsorption and desorption of hydrogen, appeared in the range of 0–0.3 V (vs RHE) (see Fig. S17 and S18 for more details). ESCAs were further calculated from the hydrogen desorption region in CVs. ESCAs of PdPt nanowires were in the range of 16–22 m²/g (Fig. 4b). Amongst them, a slightly larger ESCA was found to be 21.5 m²/g for ultrathin Pd₈₈Pt₁₄ nanowires in acid media, indicating that structural and compositional advantages contribute to more electrocatalytically active sites for adsorption and desorption of hydrogen. In contrast, the ESCAs of commercial PdNPs and PtNPs are 9.1 and 33.3 m²/g, respectively.

LSV curves, which were collected in 0.5 M H₂SO₄ with a scan rate of 5 mV/s, were utilized to investigate the HER activity of these catalysts (normalized to the geometric area of GCE). As shown in Figs. 4c and S19, the electrocatalytic activity of monometallic Pd nanowires was very weak with an onset overpotential of ~300 mV at the current density (j) of 50 mA/cm². The result indicated that monometallic Pd nanocrystal is not an ideal catalyst for HER. With introduction Pt into Pd nanowires, the activity was dramatically enhanced, even only with the doping of 1.5 at% of Pt. The overpotential of ~30 mV in 10 mA/cm²

definitely implied the key factor of Pt in HER (Fig. 4d). When with 3.5 at% of Pt, the LSV curve for Pd_{96.5}Pt_{3.5} almost overlapped to that of commercial PtNPs. Considering the lower price of Pd, ultrathin Pd_{96.5}Pt_{3.5} bimetallic nanowires may be used as an alternate candidate electrocatalyst for HER. The activity was further enhanced with increasing component of Pt, until Pd₈₆Pt₁₄ nanowires exhibited the best HER activity. However, electrocatalytic activity slightly decreased when the composition of Pt was higher than 23 at%. A similar tendency of HER activity was also observed when normalized with calculated ECSAs (Fig. S19).

To better prove the structural and compositional advantages of PdPt nanowires on HER, we further compared the electrocatalytic activity of ultrathin PdPt nanowires with monometallic Pd nanowires, commercial PdNPs and PtNPs (Fig. 5). As shown in Fig. 5a, LSV curve of ultrathin Pd₈₆Pt₁₄ bimetallic nanowires in 0.5 M H₂SO₄ exhibited a superior HER activity, following the order of PdNPs < Pd nanowires < PtNPs < Pd₈₆Pt₁₄ nanowires. The lowest overpotentials of 0.8 and 5.4 mV were observed for Pd₈₆Pt₁₄ nanowires at $j = 10$ mA/cm² and 50 mA/cm², which were 13 and 16 mV, 217 and 286 mV, and 303 and 404 mV lower than that of PtNPs, Pd nanowires, and PdNPs, respectively. Tafel plots, which were fitted from LSV curves, were further given for exploring the electrocatalytic mechanism of superior activity (Fig. 5b). A very large Tafel slope of -87.9 mV/Dec for monometallic Pd nanowires was observed, slightly smaller than that for commercial PdNPs (-177 mV/Dec). The results indicated monometallic Pd nanocrystals followed the Volmer-Tafel mechanism, in which the adsorption of hydrogen and recombination of adsorbed hydrogen together affected the electrocatalytic reaction kinetics [45]. In contrast, the very small Tafel slopes for PtNPs (-34.1 mV/Dec) and Pd₈₆Pt₁₄ nanowires (-28.8 mV/Dec) suggested quicker catalytic kinetics during HER, which followed a Volmer-Heyrovsky mechanism where the recombination of adsorbed hydrogen was the rate-limiting step [46,47]. EIS techniques, which were used in 0.5 M H₂SO₄, were further carried out to evaluate the electrocatalytic interfacial reaction kinetics during the HER electrocatalysis [46]. As shown in Fig. 5c, ultrathin Pd₈₆Pt₁₄ nanowires

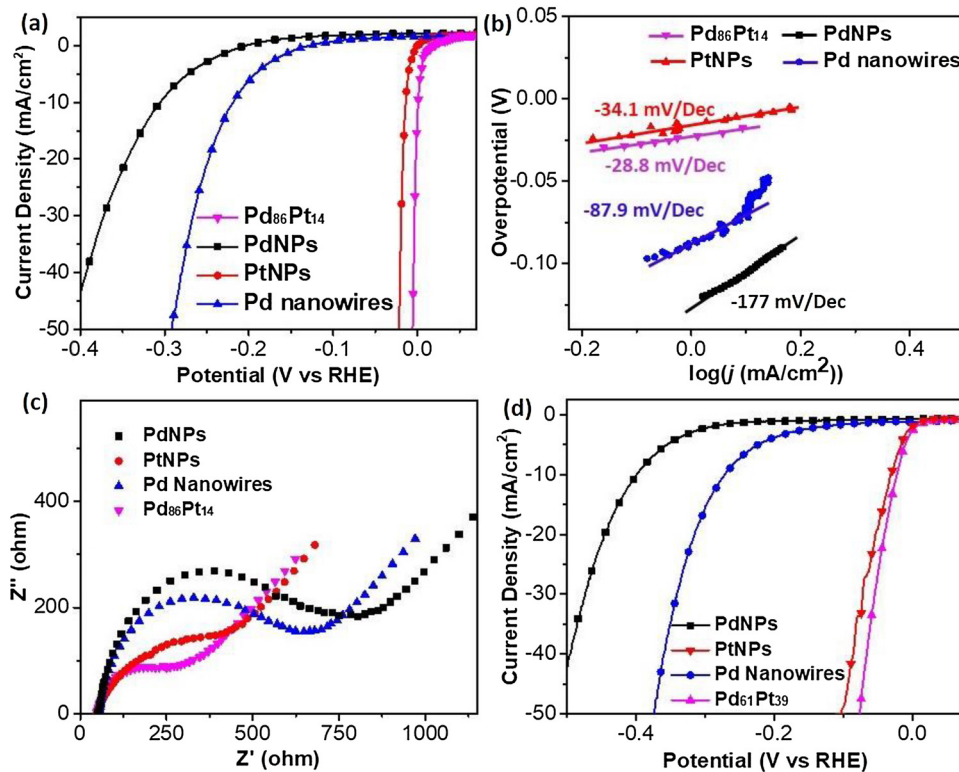


Fig. 5. Electrocatalytic performance of ultrathin Pd₈₆Pt₁₄ nanowires. (a) LSV curves, (b) corresponded Tafel plots and (c) electrochemical impedance spectra of PdNPs, PtNPs, ultrathin Pd and bimetallic Pd₈₄Pt₁₄ nanowires in 0.5 M H₂SO₄ at a scan rate of 5 mV/s. (d) LSV curves of PdNPs, PtNPs, ultrathin Pd and Pd₆₁Pt₃₉ nanowires in 1 M KOH at a scan rate of 5 mV/s.

exhibited the smallest diameter of impedance arc (DIA), following an order of Pd₈₆Pt₁₄ nanowires < PtNPs < Pd nanowires < PdNPs. The results indicated that Pd₈₆Pt₁₄ nanowires possessed the smallest charge transfer resistance and faster proton reduction kinetics for HER.

Electrocatalytic HER activity of bimetallic PdPt nanowires in alkaline media (1 M KOH) was also investigated. As shown in Fig. S20, with increasing Pt content in bimetallic PdPt nanowires, the HER activity was gradually enhanced and was best for Pd₆₁Pt₃₉ nanowires. Then, the activity slightly decreased with the higher Pt content. We further compared the LSV curve of bimetallic Pd₆₁Pt₃₉ nanowires with those of monometallic Pd nanowires as well as commercial PdNPs and PtNPs (Fig. 5d). Bimetallic Pd₆₁Pt₃₉ nanowires exhibited a superior HER activity in 1.0 M KOH, catalytically more active than commercial PtNPs and monometallic counterpart nanocatalysts. The results implied that ultrathin PdPt bimetallic nanowires were the superior electrocatalysts in both acidic and alkaline conditions [48,49].

Another severe challenge in HER is developing the electrocatalysts with superior stability. Therefore, we first investigated the stability of ultrathin Pd₈₆Pt₁₄ bimetallic nanowires by repeating 10,000 CV scans at a scan rate of 50 mV/s in a N₂-bubbled acid solution (0.5 M H₂SO₄) (Fig. 6a). No obvious change in CVs can be seen for single-crystalline Pd₈₆Pt₁₄ nanowires. We further compared the ECSA before and after CV scans. About 92.6% of initial ECSA (from 21.5–19.9 m²/g) was retained after continuous potential sweeps for 10,000 cycles, indicating the superior stability of single-crystalline Pd₈₆Pt₁₄ nanowires. No visible change in nanowire shape was observed before and after long-term CV cycling by TEM images (Figs. 6b and S21), benefitting the structural stability of anisotropic Pd₈₆Pt₁₄ nanowires. In contrast, commercial PtNPs only retained 63.4% of initial ECSA after 10,000 cycles, which has also been confirmed by the visible aggregates of commercial PtNPs in nanostructures (Fig. S22). Similarly, negligible shifts in LSV curves (only 0.7 mV loss in $j = 10 \text{ mA}/\text{cm}^2$) before and after the long-term CV cycling also confirmed the superior stability of anisotropic Pd₈₆Pt₁₄ nanowires, compared to that of spherical PtNPs (5.3 mV) (Fig. 5c). The current-time ($i-t$) chronoamperometric responses finally revealed that bimetallic Pd₈₆Pt₁₄ nanowires only underwent a slight loss of current

density (only 4.6%) for 26 h (Fig. 5d). In contrast, only 63.9%, and 56.1% of current retention was maintained for PdNPs and PtNPs, respectively.

Based on these observations, the enhanced HER performance (activity and stability) of ultrathin single-crystalline PdPt bimetallic nanowires could be ascribed to a combined result of an electronic synergistic effect and structurally ultrathin anisotropy. On the one hand, bimetallic PdPt nanowires effectively modified their electronic crystal structure; the formation of Pd-Pt interactions possibly decreased the binding energy of adsorbed hydrogen and enhanced the activity during electrocatalytic HER. The similar phenomenon was also observed from other bimetallic nanostructures, in which doping secondary metals can enhance the electrocatalytic activity in HER [50], ORR [10,51,52], and oxidation of small molecules (methanol, ethanol and glucose) [41,53,54]. On the other hand, anisotropic single-crystalline ultrathin 1D nanostructures provided more exposed active sites, easier electron transfer, and high utilization efficiency on crystal surfaces for HER. This structural feature was definitely confirmed by our control experiments that ultrathin Pd nanowires exhibited enhanced electrocatalytic activity and stability, compared to their counterparts with 0D particle nanostructures.

4. Conclusions

In summary, a facile solution-phase method was developed to synthesize ultrathin PdPt bimetallic nanowires *in situ* based on a surfactant-directing approach. Mechanistic studies revealed that Pd played a key role in the synthesis of 1D bimetallic PdPt nanowires with tunable components. The resultant PdPt nanowires exhibited a dramatically enhanced electrocatalytic activity and stability towards HER under both acid and base conditions, thanks to the 3-nm-thick ultrathin diameter, anisotropic 1D single-crystalline nanostructure (100–300 nm), and bimetallic composition. We expect this work offers a general surfactant-directing strategy to control the anisotropic nanostructures in diverse bimetallic nanomaterials, and presents a chance to rationally design highly efficient and stable electrochemical nanocatalysts.

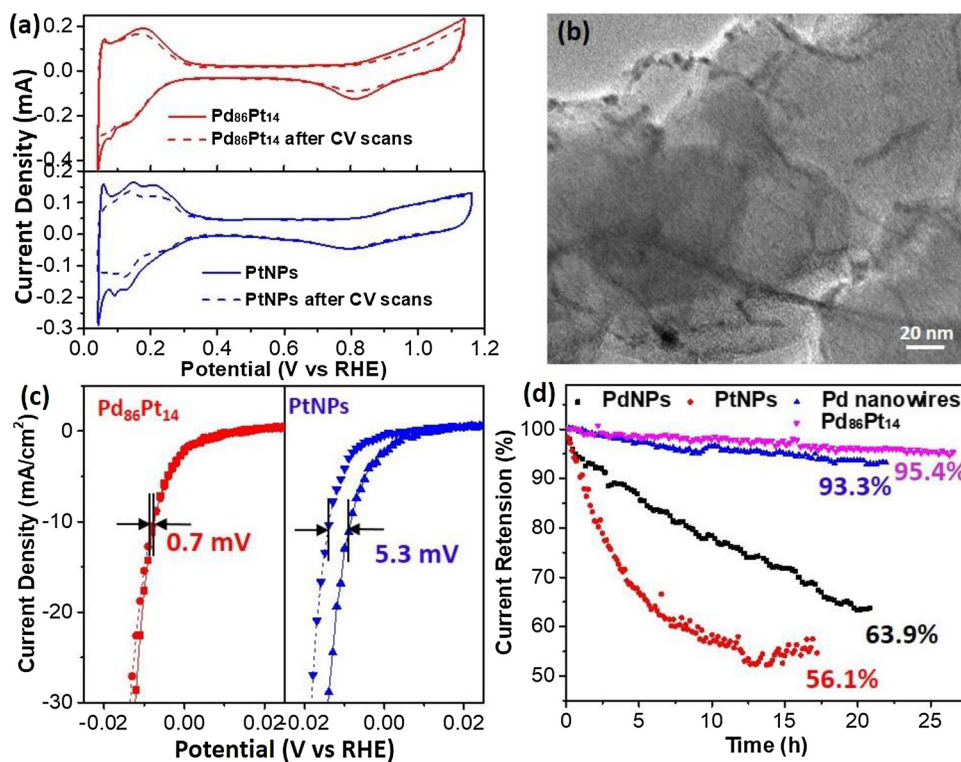


Fig. 6. Electrocatalytic stability of ultrathin PdPt bimetallic nanowires in 0.5 M H₂SO₄. (a) CV curves of ultrathin Pd₈₆Pt₁₄ nanowires and commercial state-of-the-art PtNPs before and after repeating CV scans of 10,000 cycles with a scan rate of 50 mV/s. (b) Typical TEM images of ultrathin Pd₈₆Pt₁₄ nanowires supported on activated carbon after CV scans. (c) LSV curves of Pd₈₆Pt₁₄ nanowires and PtNPs before and after CV scans. (d) Time-dependent *i-t* curves of monometallic Pd and bimetallic Pd₈₆Pt₁₄ nanowires as well as commercial PdNPs and PtNPs at 50 mA/cm².

Acknowledgements

This work was supported by National Natural Science Foundation of China (No. 21501095), Jiangsu Specially Appointed Professor plan, Natural Science Foundation of Jiangsu Province (No. BK20150969), the research fund from Priority Academic Program Development of Jiangsu Higher Education Institutions, National and Local Joint Engineering Research Center of Biomedical Functional Materials. SLS thanks the US Department of Energy for support of this work under grant DE-FG02-86ER13622.A000.

Appendix A. Supplementary data

Supplementary material related to this article can be found, in the online version, at doi:<https://doi.org/10.1016/j.apcatb.2018.07.060>.

References

- [1] C. Bianchini, P.K. Shen, Chem. Rev. 109 (2009) 4183–4206.
- [2] J.N. Tiwari, R.N. Tiwari, K.S. Kim, Prog. Mater. Sci. 57 (2012) 724–803.
- [3] Y. Xu, B. Zhang, Chem. Soc. Rev. 43 (2014) 2439–2450.
- [4] A. Chen, C. Ostrom, Chem. Rev. 115 (2015) 11999–12044.
- [5] K.D. Gilroy, A. Ruditskiy, H.-C. Peng, D. Qin, Y. Xia, Chem. Rev. 116 (2016) 10414–10472.
- [6] C. Zhu, D. Du, A. Eychmuller, Y. Lin, Chem. Rev. 115 (2015) 8896–8943.
- [7] W. Yu, M.D. Porosoff, J.G. Chen, Chem. Rev. 112 (2012) 5780–5817.
- [8] H.H. Li, S.Y. Ma, Q.Q. Fu, X.J. Liu, L. Wu, S.H. Yu, J. Am. Chem. Soc. 137 (2015) 7862–7868.
- [9] B. Lim, M. Jiang, P.H. Camargo, E.C. Cho, J. Tao, X. Lu, Y. Zhu, Y. Xia, Science 324 (2009) 1302–1305.
- [10] N. Jung, D.Y. Chung, J. Ryu, S.J. Yoo, Y.-E. Sung, Nano Today 9 (2014) 433–456.
- [11] H.-P. Liang, H.-M. Zhang, J.-S. Hu, Y.-G. Guo, L.-J. Wan, C.-L. Bai, Angew. Chem. 116 (2004) 1566–1569.
- [12] J. Lai, S. Guo, Small 2017, 1702156.
- [13] M. Smiljanic, Z. Rakocevic, A. Maksic, S. Strbac, Electrochim. Acta 117 (2014) 336–343.
- [14] Y. Liu, M. Chi, V. Mazumder, K.L. More, S. Soled, J.D. Henao, S. Sun, Chem. Mater. 23 (2011) 4199–4203.
- [15] C. Zhu, S. Guo, S. Dong, Adv. Mater. 24 (2012) 2326–2331.
- [16] Y. Zheng, Y. Jiao, M. Jaroniec, S.Z. Qiao, Angew. Chem. Int. Ed. 54 (2015) 52–65.
- [17] H. Huang, K. Li, Z. Chen, L. Luo, Y. Gu, D. Zhang, C. Ma, R. Si, J. Yang, Z. Peng, J. Zeng, J. Am. Chem. Soc. 139 (2017) 8152–8159.
- [18] L. Zhang, L.T. Roling, X. Wang, M. Vara, M. Chi, J. Liu, S.-I. Choi, J. Park, J.A. Herron, Z. Xie, M. Mavrikakis, Y. Xia, Science 349 (2015) 412–416.
- [19] C. Chen, Y. Kang, Z. Huo, Z. Zhu, W. Huang, H.L. Xin, J.D. Snyder, D. Li, J.A. Herron, M. Mavrikakis, M. Chi, K.L. More, Y. Li, N.M. Markovic, G.A. Somorjai, P. Yang, V.R. Stamenkovic, Science 343 (2014) 1339–1343.
- [20] X. Zhao, S. Chen, Z. Fang, J. Ding, W. Sang, Y. Wang, J. Zhao, Z. Peng, J. Zeng, J. Am. Chem. Soc. 137 (2015) 2804–2807.
- [21] L. Ruan, E. Zhu, Y. Chen, Z. Lin, X. Huang, X. Duan, Y. Huang, Angew. Chem. Int. Ed. 52 (2013) 12577–12581.
- [22] X. Huang, N. Zheng, J. Am. Chem. Soc. 131 (2009) 4602–4603.
- [23] L. Bu, J. Ding, S. Guo, X. Zhang, D. Su, X. Zhu, J. Yao, J. Guo, G. Lu, X. Huang, Adv. Mater. 27 (2015) 7204–7212.
- [24] Y. Ma, W. Gao, H. Shan, W. Chen, W. Shang, P. Tao, C. Song, C. Addiego, T. Deng, X. Pan, J. Wu, Adv. Mater. (2017) 29.
- [25] B.Y. Xia, H.B. Wu, Y. Yan, X.W. Lou, X. Wang, J. Am. Chem. Soc. 135 (2013) 9480–9485.
- [26] L. Cademartiri, G.A. Ozin, Adv. Mater. 21 (2009) 1013–1020.
- [27] Y. Xia, P. Yang, Y. Sun, Y. Wu, B. Mayers, B. Gates, Y. Yin, F. Kim, H. Yan, Adv. Mater. 15 (2003) 353–389.
- [28] Y. Lu, S. Du, R. Steinberger-Wilckens, Appl. Catal. B Environ. 199 (2016) 292–314.
- [29] Y. Kang, X. Ye, J. Chen, Y. Cai, R.E. Diaz, R.R. Adzic, E.A. Stach, C.B. Murray, J. Am. Chem. Soc. 135 (2013) 42–45.
- [30] H. Zhang, M. Jin, J. Wang, W. Li, P.H.C. Camargo, M.J. Kim, D. Yang, Z. Xie, Y. Xia, J. Am. Chem. Soc. 133 (2011) 6078–6089.
- [31] M. Chen, B. Wu, J. Yang, N. Zheng, Adv. Mater. 24 (2012) 862–879.
- [32] X. Huang, Y. Li, Y. Chen, E. Zhou, Y. Xu, H. Zhou, X. Duan, Y. Huang, Angew. Chem. Int. Ed. 52 (2013) 2520–2524.
- [33] X. Teng, W.-Q. Han, W. Ku, M. Hücker, Angew. Chem. 120 (2008) 2085–2088.
- [34] C. Burda, X. Chen, R. Narayanan, M.A. El-Sayed, Chem. Rev. 105 (2005) 1025–1102.
- [35] Q. Fan, K. Liu, Z. Liu, H. Liu, L. Zhang, P. Zhong, C. Gao, Part. Part. Syst. Charact. 34 (2017) 1700075.
- [36] M. Lukaszewski, M. Soszko, A. Czerwiński, Int. J. Electrochem. Sci. 11 (2016) 4442–4469.
- [37] S.H. Han, H.M. Liu, P. Chen, J.X. Jiang, Y. Chen, Adv. Energy Mater. (2018) 1801326.
- [38] D. Xu, X. Liu, M. Han, J. Bao, Chem. Commun. 52 (2016) 12996–12999.
- [39] D. Xu, X. Liu, H. Lv, Y. Liu, S. Zhao, M. Han, J. Bao, J. He, B. Liu, Chem. Sci. 9 (2018) 4451–4455.
- [40] Y. Liu, M. Chi, V. Mazumder, K.L. More, S. Soled, J.D. Henao, S. Sun, Chem. Mater. 23 (2011) 4199–4203.
- [41] C. Zhu, S. Guo, S. Dong, Adv. Mater. 24 (2012) 2326–2331.
- [42] Y.-W. Lee, A.-R. Ko, S.-B. Han, H.-S. Kim, K.-W. Park, Phys. Chem. Chem. Phys. 13 (2011) 5569–5572.
- [43] W. Hong, C. Shang, J. Wang, E. Wang, Energy Environ. Sci. 8 (2015) 2910–2915.
- [44] M. Khan, A.B. Yousa, M. Chen, C. Wei, X. Wu, N. Huang, Z. Qi, L. Li, J. Power Sources 282 (2015) 520–528.
- [45] S. Štrbac, M. Smiljanic, Z. Rakočević, J. Electroanal. Chem. 755 (2015) 115–121.

- [46] B. Liu, L. Jin, W. Zhong, A. Lopes, S.L. Suib, J. He, *Chem. Eur. J.* 24 (2018) 2565–2569.
- [47] B.E. Conway, B.V. Tilak, *Electrochim. Acta* 47 (2002) 3571–3594.
- [48] L. Zhang, Q. Chang, H. Chen, M. Shao, *Nano Energy* 29 (2016) 198–219.
- [49] M. Smiljanic, Z. Rakocevic, A. Maksic, S. Strbac, *Electrochim. Acta* 117 (2014) 336–343.
- [50] J. Greeley, J.K. Nørskov, L.A. Kibler, A.M. El-Aziz, D.M. Kolb, *ChemPhysChem* 7 (2006) 1032–1035.
- [51] H. Huang, K. Li, Z. Chen, L. Luo, Y. Gu, D. Zhang, C. Ma, R. Si, J. Yang, Z. Peng, *J. Am. Chem. Soc* 139 (2017) 8152–8159.
- [52] K. Jiang, Q. Shao, D. Zhao, L. Bu, J. Guo, X. Huang, *Adv. Funct. Mater.* 27 (2017) 1700830.
- [53] Y. Liu, M. Chi, V. Mazumder, K.L. More, S. Soled, J.D. Henao, S. Sun, *Chem. Mater.* 23 (2011) 4199–4203.
- [54] B.A. Kakade, T. Tamaki, H. Ohashi, T. Yamaguchi, *J. Phys. Chem. C* 116 (2012) 7464–7470.